Published in final edited form as:
Neuron. 2019 December 18; 104(6): 1153–1167.e4. doi:10.1016/j.neuron.2019.09.023.

Thalamic input to orbitofrontal cortex drives brain-wide, frequency-dependent inhibition mediated by GABA and zona incerta

Andrew J. Weitz[#1,2], **Hyun Joo Lee**[#2], **ManKin Choy**[2], **Jin Hyung Lee**[1,2,3,4,6,*]

[1]Department of Bioengineering, Stanford University, Stanford, CA 94305, USA

[2]Department of Neurology and Neurological Sciences, Stanford University, Stanford, CA 94305, USA

[3]Department of Neurosurgery, Stanford University, Stanford, CA 94305, USA

[4]Department of Electrical Engineering, Stanford University, CA 94305, USA

[#] These authors contributed equally to this work.

SUMMARY

Anatomical and behavioral data suggest that the ventrolateral orbitofrontal cortex (VLO), which exhibits extensive connectivity and supports diverse sensory and cognitive processes, may exert global influence over brain activity. However, this hypothesis has never been tested directly. We applied optogenetic fMRI to drive various elements of VLO circuitry while visualizing the whole-brain response. Surprisingly, driving excitatory thalamocortical projections to VLO at low frequencies (5–10 Hz) evoked widespread, bilateral decreases in brain activity spanning multiple cortical and subcortical structures. This pattern was unique to thalamocortical projections, with direct stimulations of neither VLO nor thalamus eliciting such a response. High-frequency stimulations (25–40 Hz) of thalamocortical projections evoked dramatically different – though still far-reaching – responses, in the form of widespread ipsilateral activation. Importantly, decreases in brain activity evoked by low-frequency thalamocortical input were mediated by GABA and activity in zona incerta. These findings identify specific circuit mechanisms underlying VLO control of brain-wide neural activities.

---

[*] **Corresponding Author and Lead Contact:** Jin Hyung Lee, PhD, ljinhy@stanford.edu, 318 Campus Drive, #W300A, Stanford, CA 94305.

[6] Lead Contact

AUTHOR CONTRIBUTIONS

AJW and JHL designed the study and wrote the paper. AJW performed fMRI experiments, data analysis, and immunohistochemistry. HJL helped with experimental design and performed electrophysiology and data analysis. MKC aided with immunohistochemistry, microscopy, and data analysis. JHL supervised AJW, HJL, and MKC throughout the study.

DECLARATION OF INTERESTS

AJW is a shareholder of LVIS. HJL is an employee and shareholder of LVIS. JHL is a founder, consultant, and board member of LVIS. AJW, HJL, and JHL are inventors of a pending patent titled, “Methods for functional brain circuit analysis.”

INTRODUCTION

The orbitofrontal cortex (OFC) has been implicated in diverse cognitive and emotional functions (Izquierdo, 2017; Price, 2007; Stalnaker et al., 2015). The ventrolateral orbital cortex (VLO), one of five sectors within OFC, stands out for supporting many of these functions (Hardung et al., 2017). Thalamic input to VLO plays a key role in modulating perceived pain levels during noxious stimuli (Huang et al., 2001; Zhang et al., 1998; Zhang et al., 1997) and supports goal-directed behavior by signaling predictive cues and expected outcome (Alcaraz et al., 2015). Neuroimaging studies suggest that VLO activity is linked to states of consciousness (Englot et al., 2009b). Additionally, the VLO is linked to spatial navigation and attention (Corwin et al., 1994; Feierstein et al., 2006; King et al., 1989), depression (Chen et al., 2012; Lin et al., 2012; Xing et al., 2011), memory formation (Zhao et al., 2013), and risk assessment (Eshel et al., 2007).

The broad involvement of VLO across cognitive and behavioral processes suggests that it influences multiple brain-wide circuits. This is supported anatomically by the region’s extensive connectivity. As the target of thalamic input from submedial and mediodorsal nuclei (Groenewegen, 1988; Reep et al., 1996; Yoshida et al., 1992), VLO is well situated to receive ascending sensory information and emotion-laden information from the limbic system. Cortical afferents also allow VLO to integrate information related to diverse processes (Reep et al., 1996). These connections, along with extensive efferent projections (Bedwell et al., 2014; Coffield et al., 1992; Craig Jr et al., 1982; Schilman et al., 2008; Shammah-Lagnado et al., 1985), suggest that VLO may act as a global hub, modulating activity across brain circuits.

Despite evidence that VLO has a global role in brain function, the circuit mechanisms by which it accomplishes such influence have not been studied directly. To better understand how VLO supports different behavioral processes, a technical approach is needed capable of controlling individual circuit elements while visualizing the brain-wide response. We applied optogenetic fMRI (ofMRI) – the combination of optogenetic stimulation with whole-brain functional magnetic resonance imaging – to directly visualize the global influence of VLO’s afferent and efferent connections. The firing rate of VLO has been shown to convey important information, reaching rates as high as 50 Hz during noxious stimuli (Backonja and Miletic, 1991; Feierstein et al., 2006; Follett and Dirks, 1995; Snow et al., 1992a). We therefore characterized how different temporal patterns of activity in the VLO circuit affect brain dynamics by driving its input and output at distinct frequencies.

RESULTS

We first investigated the influence of thalamocortical projections to VLO by stimulating thalamic terminals there. Adenoassociated virus carrying the ChR2-EYFP excitatory opsin was injected into the submedial nucleus of thalamus (Figure 1A). To achieve targeted transfection, we used the CaMKIIa promoter, which in thalamus is primarily expressed in excitatory relay neurons (Smith, 2008). This resulted in strong membrane-bound expression of ChR2 at the site of injection (Figure S1A). E*x vivo* histology confirmed that ChR2 was strongly expressed in layers I and III of VLO (Figure S1B,C), consistent with known termination patterns of the injected nucleus (Krettek and Price, 1977). Stimulation of ChR2-positive terminals in cortex was achieved by implanting an optical fiber in VLO (Figure 1A).

Optogenetic fMRI experiments were conducted in order to visualize the dynamic, brain-wide response to different frequencies of thalamocortical stimulation. Optical pulses were delivered at a frequency of 10 or 40 Hz. Imaging was performed over 23 coronal slices (Figure 1B). Standard general linear model (GLM) statistical techniques were used to identify voxels significantly modulated during stimulation (Figure 1C). Responses were highly consistent across scans and subjects (Figure S2).

Frequency of thalamocortical stimulation in VLO controls interhemispheric modulation

fMRI activation maps show that stimulation frequency was a critical parameter in determining the spatial extent of ipsilateral and contralateral modulation (Figure 1D,E). Both stimulation frequencies resulted in a robust positive response at the site of stimulation in VLO, as well as in the ipsilateral thalamus and striatum. 10 Hz stimulation drove a bilateral negative response that spanned across cortex, contralateral striatum, and contralateral thalamus. 40 Hz stimulation caused robust positive activations throughout ipsilateral cortex, but the contralateral hemisphere was mostly devoid of any modulation. Only a marginal negative response in prefrontal cortex and striatum was observed.

To quantify response patterns, we calculated the number of significantly modulated voxels in anatomically defined regions of interest (ROIs; Figure S3A). In the ipsilateral hemisphere, the number of modulated voxels increased between 10 and 40 Hz for all segmented areas of cortex and striatum (Figure S3B; $p < 0.05$, N=11 animals). Conversely, in the contralateral hemisphere, the amount of modulated volume decreased between 10 and 40 Hz (Figure S3D). These results indicate that the firing rate of thalamic input to VLO determines the spatial extent of downstream modulation. The ipsilateral hemisphere is modulated most during 40 Hz stimulation, while the contralateral hemisphere is modulated most during 10 Hz stimulation. The same frequency-dependent trends were observed when a constant pulse width was used in control experiments (Figure S4A,B).

Frequency of thalamocortical stimulation in VLO controls the polarity of evoked responses

We next examined the temporal dynamics of brain-wide responses. Quantitative measurements of each ROI's response polarity were calculated as the sum of its average fMRI time series (∑fMRI). In the ipsilateral hemisphere, sensory, cingulate, and motor cortex exhibited a significant negative response during 10 Hz stimulation (Figure S3C; $p < 0.05$, N=11 animals). These same regions, with striatum, LPFC, and MPFC, exhibited a significant positive response during 40 Hz stimulation. Visualizing the time series throughout ipsilateral cortex largely corroborated ∑fMRI measurements (Figure 1F). Sensory, cingulate, and motor cortex all displayed a robust negative response during 10 Hz stimulation that switched to positive during 40 Hz stimulation.

Quantitative measurements of ∑fMRI in the contralateral hemisphere varied greatly from those observed in the ipsilateral hemisphere. The cortex and striatum exhibited significant negative responses during 10 Hz stimulation (Figure S3E; $p < 0.05$, N=11 animals), but no ∑fMRI values were significantly different from zero during 40 Hz stimulation.

Visualizing the time series throughout contralateral cortex confirmed that activity there sharply decreased during 10 Hz stimulation (Figure 1G). fMRI responses to 40 Hz stimulation were generally flat or – in the case of LPFC – displayed a minor negative deflection. These data illustrate the widespread, bilateral influence that thalamic inputs to VLO exert by suppressing remote activity in a frequency-dependent manner. Importantly, this effect was preserved when pulse width was held constant in control experiments (Figure S4C,D), confirming that stimulation frequency was the primary factor in determining the polarity of stimulus-evoked responses.

Frequency sweep experiments reveal region-dependent transitions in response patterns

In order to explore how frequency-dependent changes manifest, we conducted a second series of imaging sessions with a subset of animals reported above (N=7). Stimulations were performed over frequencies ranging from 5 to 40 Hz in 5 Hz intervals. The resulting activation maps are shown in Figure 2A. Stimulation at all frequencies evoked a positive response at the site of stimulation. The negative response observed throughout the contralateral hemisphere during 10 Hz stimulation was observed from 5 Hz to frequencies as high as 20 Hz. At 25 Hz and above, negative responses in the contralateral hemisphere were generally limited to prefrontal cortex. Interestingly, it was also at 25 Hz that widespread activation of the ipsilateral cortex started to manifest. To quantify this effect, we examined the percentage of voxels that were significantly modulated at each frequency (Figure 2B). Several regions exhibited a large increase in positive modulation volume between 20 and 25 Hz, suggesting that a threshold for widespread forebrain activation had been reached. Negative modulation volumes were also greater during 5 Hz stimulation compared to 10 Hz stimulation, suggesting that the circuit mechanism responsible for negative signals has an even stronger effect at lower frequencies. Notably, the transition from negative to positive responses observed in sensory, motor, and cingulate cortex occurred between 10 and 15 Hz stimulation. Time series extracted from these ROIs confirmed this trend (Figure 2C).

Thalamocortical projections to VLO uniquely drive widespread negative fMRI signals

The thalamocortical projections to VLO represent only one neuronal element in the perturbed circuit. To better understand the source of fMRI responses, we also stimulated pyramidal neurons in VLO. Neither 10 nor 40 Hz stimulation of cell bodies in VLO drove a negative fMRI response in any region (Figure 3A,B). Similar to stimulation of thalamocortical projections, exciting cell bodies at 40 Hz drove activation of the ipsilateral thalamus. However, the widespread cortical activations observed during stimulation of thalamocortical projections did not occur. These data suggest that direct activation of VLO does not cause the same frequency-dependent or widespread inhibitory effects induced by thalamic input to this region. We next stimulated cell bodies in the thalamic submedial nucleus, which projects heavily to VLO. As shown in the group-level activation maps (Figure 3C,D), driving these relay neurons at 10 and 40 Hz elicits a strong response in VLO, but fails to evoke a negative fMRI response in any region. Thus, directly stimulating the projections to VLO elicits a fundamentally different response than stimulating cell bodies that project there.

Neuronal underpinnings of brain-wide, frequency-dependent fMRI signals

Across the brain, we observed several classes of frequency-dependent fMRI responses during stimulation of thalamic input to VLO (Figure 1). To investigate how these dynamics relate to neuronal activity, we performed a series of *in vivo* electrophysiology experiments. We first performed extracellular recordings at the site of stimulation in ipsilateral VLO (Figure 4A), where the fMRI response was positive during stimulation at both 10 and 40 Hz (Figure 4B). Peri-event time histograms from a representative unit show that these signal changes were associated with corresponding increases in spiking (Figure 4C). Across all recorded units, over half were modulated by stimulation at either frequency (Figure 4D and S5A; 60% and 54% during 10 and 40 Hz stimulation, respectively; N=151 units, 5 animals, 10 trials per frequency). Furthermore, nearly all modulated units exhibited a significant increase in firing rate (99% and 96%, respectively). The median change in firing rate was not significantly different between the two frequencies (Figure 4E). These results confirm that positive fMRI signals observed at the site of stimulation reflect underlying increases in neuronal activity.

We next investigated whether the negative fMRI signals observed throughout contralateral cortex during 10 Hz stimulation reflect underlying decreases in neuronal activity, and whether this modulation is suppressed at higher stimulation frequencies as suggested by fMRI. Extracellular recordings were performed in contralateral VLO (cVLO; Figure 4F), where a negative fMRI signal was observed during 10 Hz stimulation, but little modulation was observed during 40 Hz stimulation (Figure 4G). Peri-event time histograms from a representative unit in cVLO confirm that this pattern was observed at the level of single unit activity (Figure 4H). Over all recorded units, 95% exhibited a significant decrease in firing rate during 10 Hz stimulation (Figure 4I and S5B; N=55 units, 2 animals, 20 trials per frequency). During 40 Hz stimulation, 78% of recorded units exhibited no significant change, and only 18% exhibited a significant decrease in activity. The median change in firing rate was significantly different between the two frequencies (Figure 4J). These results confirm that low frequencies of thalamic input to VLO preferentially drive decreases in neuronal spiking in the contralateral cortex.

Finally, we examined whether the frequency-dependent switch in fMRI polarity observed in ipsilateral cortex was associated with corresponding changes in neuronal activity. We therefore performed recordings in the ipsilateral motor cortex (Figure 4K), where a negative fMRI signal was observed during 10 Hz stimulation, but a positive signal was evoked during 40 Hz stimulation (Figure 4L). Peri-event time histograms from a representative unit show that this behavior was consistent with underlying spiking dynamics (Figure 4M). Across all recorded units, 46% exhibited a significant decrease in firing rate during 10 Hz stimulation (Figure 4N and S5C; N=99 units, 4 animals, 20 trials per frequency) with the remaining units showing no significant change. During 40 Hz stimulation, 82% of recorded units exhibited a significant increase in firing rate and none exhibited a significant decrease. The median change in firing rate was significantly different between the two frequencies (Figure 4O). These data confirm that the frequency-dependent switch in cortical response polarity measured with fMRI reflects underlying spiking activity.

Mechanisms of evoked decreases in cortical activity

Having established that negative fMRI signals in cortex reflect a decrease in neuronal spiking, we sought to identify the mechanism for this frequency-dependent response. We hypothesized that the thalamic reticular nucleus (TRN) might play a role, since it directly inhibits thalamic nuclei and can suppress excitatory input to cortex (Lewis et al., 2015; Pinault, 2004). To examine whether activity in TRN was correlated with decreases in cortical firing, we performed extracellular recordings there during 10 and 40 Hz thalamocortical stimulation (Figure S6A). Given the frequency-dependent nature of evoked decreases in cortical activity, we predicted that 10 Hz stimulation would evoke the strongest response in TRN. However, the percentage of units exhibiting a significant increase in firing rate more than doubled between 10 and 40 Hz stimulation (Figure S6B; 25% and 69%, respectively; N=123 units, 2 animals, 10–20 trials per frequency). The median change in firing rate across recorded units was significantly different between the two frequencies, with 40 Hz stimulation driving greater changes (Figure S6C,D). To investigate whether bilateral pathways were involved, we performed recordings in the contralateral reticular nucleus (Figure S6E). During 10 Hz stimulation, 54% of units there were modulated, of which 98% exhibited a significant decrease in firing rate (Figure S6F, N=199 recorded units, 20 trials per frequency). During 40 Hz stimulation, 13% of units were modulated, of which 80% exhibited a significant increase in firing rate. Over all recorded units, the median change in firing rate was significantly different between the two frequencies, with 40 Hz stimulation again driving greater changes (Figure S6G,H). These data suggest that inhibition from TRN onto thalamus is not a major cause of the decreases in cortical activity observed during low-frequency thalamocortical stimulation.

We next hypothesized that decreases in cortical activity reflect direct GABA-mediated inhibition. We therefore tested the dependence of this response on downstream GABA release by comparing evoked changes in firing rate before and after micro-infusion of bicuculline methiodide (BMI). Although BMI can exhibit mixed pharmacological effects (e.g. blockage of calcium-activated potassium channels), it is a strong antagonist of GABA_A receptors. Single-unit recordings were performed in cVLO, where negative fMRI signals were observed during 10 Hz thalamocortical stimulation (Figure 5A). To ensure that any changes associated with BMI infusion were due to its pharmacological effect, we first performed infusions with sterile saline. To inject both BMI and saline, a pair of cannulas was attached to the recording electrode directly above the electrical contacts (Figure 5B).

In line with expectations, saline infusion had a negligible effect on cortical inhibition evoked by 10 Hz stimulation. Among 49 units recorded in cVLO, 94% exhibited a significant decrease in firing rate during 10 Hz stimulation both before and after saline infusion (Figure 5C; N=2 animals, 20 trials per condition). Furthermore, saline infusion did not have a significant effect on the median change in firing rate evoked by 10 Hz stimulation (Figure 5D). In contrast, infusion of BMI completely eliminated the stimulus-evoked inhibition (Figure 5C). Prior to BMI infusion, 10 Hz stimulation evoked a significant decrease in firing rate in 86% of units. After BMI infusion, the recorded units were either not modulated by stimulation (96%) or exhibited a significant increase in firing rate (4%). The median change in firing rate evoked by stimulation was also significantly different (Figure 5D). Importantly, the baseline firing rate in cVLO did not change following BMI infusion in a majority of units (Figure 5E). Those that did exhibit a difference were roughly split between increases (27%) and decreases (18%). Furthermore, across all units, the average baseline firing rate was not significantly different after BMI infusion (p=0.66). These analyses suggest the drug's effect was related to stimulus-evoked GABA release and not a general decrease in local inhibitory action. The reduction in stimulus-evoked inhibition took immediate effect after BMI infusion and continued throughout the following twenty trials (Figure 5F). Peri-event time histograms from a representative unit illustrate how stimulus-evoked decreases in firing rate were observed after saline infusion but eliminated after BMI infusion (Figure 5G). These findings suggest that the widespread cortical inhibition driven by low-frequency thalamic input to VLO is mediated by the release of GABA at remote sites downstream from excited terminals.

Cortical inhibition driven by thalamic input to VLO is mediated by zona incerta

Having established that GABA drove decreases in cortical activity, we sought to identify potential sources of the inhibitory neurotransmitter and investigated the role of zona incerta (ZI). In addition to receiving collaterals of the stimulated projection and sparse input from VLO (Kuramoto et al., 2017; Shammah-Lagnado et al., 1985), the ZI sends bilateral GABAergic projections throughout neocortex (Lin et al., 1990) and has previously been shown to mediate cortical decreases in firing rate resulting from 10 Hz thalamic stimulation (Liu et al., 2015). To examine whether this region mediated the widespread inhibition observed throughout forebrain, we inactivated its activity during simultaneous 10 Hz thalamocortical stimulations and recordings in cVLO.

ZI activity was first inactivated via incertal infusions of the sodium channel blocker lidocaine hydrochloride (Figure 6A and S7A,B). Incertal saline infusion did not affect the remote inhibition driven by 10 Hz stimulation. At least 98% of units recorded in cVLO exhibited a significant decrease in firing rate during stimulation both prior to and after saline infusion (Figure 6B; N=62 units, 20 trials per condition). In contrast, only 72% of units were inhibited during 10 Hz stimulation after inactivation of zona incerta with lidocaine (Figure 6B). The median change in firing rate evoked by stimulation was also significantly different between the three conditions (Figure 6D, $p=1.1\times10^{-12}$, $\chi^2=55.0$, 185 degrees of freedom). Post-hoc tests confirmed that stimulus-evoked changes after saline infusion were not different than baseline values (p=0.17), while stimulus-evoked changes after lidocaine infusion were different than both baseline and post-saline values ($p=9.6\times10^{-10}$ and 3.0×10^{-7}, respectively). The reduction in evoked inhibition took immediate effect after lidocaine infusion and persisted throughout the following twenty trials (Figure 6C). Peri-event time histograms from a representative unit show that in a subset of recorded units, incertal infusions of lidocaine, but not saline, completely eliminated the remote cortical inhibition driven by 10 Hz stimulation (Figure 6E).

To confirm the role of ZI in mediating remote cortical inhibition, we performed a similar experiment using the inhibitory opsin eNpHR. In addition to the normal ChR2-EYFP injection into thalamus, adeno-associated virus carrying eNpHR-mCherry controlled by the pan-neuronal hSyn promoter was injected into zona incerta (Figure S7D). This enabled robust suppression of incertal activity (Figure S7E–G). To assess the role of ZI in remote inhibition, single-unit recordings were performed within cVLO and zona incerta during 10 Hz stimulation with and without concurrent eNpHR activation (Figure 7A). These stimulation patterns were interleaved to ensure that differences between them could be attributed to eNpHR activation (Figure 7B). Optrode placement in zona incerta was validated by confirming that the recorded population responded to contralateral whisker stimulation, a property that ZI is known to possess (Nicolelis et al., 1992) (Figure S7C).

Among 26 units recorded in zona incerta, 65% exhibited a significant increase in firing rate during 10 Hz thalamocortical stimulation (Figure 7C,G). Thus, zona incerta was recruited during the stimulation paradigm that drove widespread inhibition. Concurrent activation of eNpHR during thalamocortical stimulation disrupted this recruitment. In 96% of recorded units, the firing rate during 10 Hz stimulation was actually less than pre-stimulus levels (Figure 7C,G). The median change in incertal firing rate during 10 Hz stimulation was also significantly different between eNpHR and non-eNpHR trials (Figure 7E).

To determine whether disruption of ZI recruitment affected the remote inhibition driven by thalamocortical stimulation, we quantified the change in cVLO’s firing rate during eNpHR and non-eNpHR trials. 67% of units exhibited a significant decrease in firing rate during 10 Hz thalamocortical stimulation (Figure 7D,H, N=18 units, 10 trials). Strikingly, suppression of ZI activity with eNpHR reversed this effect. No units exhibited a significant change in firing rate when 10 Hz stimulation was paired with eNpHR activation (Figure 7D,H). The median change in firing rate across recorded units was also significantly different between the two conditions (Figure 7F). Collectively, these data confirm that zona incerta mediates inhibition in at least one downstream region driven by low-frequency input to VLO.

To confirm the role of ZI in mediating inhibition, we investigated the effect of suppressing its activity alone on cortical firing (i.e. without thalamocortical stimulation). Recordings were performed in cVLO (Figure S7H), where a majority of units (N=22/24, 92%) exhibited no significant change during inhibition of zona incerta (Figure S7I). The remaining 8% exhibited a small but significant increase in firing rate. These data suggest that any tonic inhibition provided by ZI over cortex is not enough to account for the large decreases in firing rate that occur during thalamocortical stimulation. As such, the role of zona incerta in mediating the observed inhibition must be specifically linked to VLO afferent stimulation.

DISCUSSION

Role of ZI in mediating cortical inhibition

Neuronal inhibition is a critical feature of normal information processing in cortex (Isaacson and Scanziani, 2011). Understanding the ways in which neuronal circuits distribute inhibition is therefore important for a broader understanding of cortical function. Given the proximal influence of interneurons in cortex (Fino and Yuste, 2011; Holmgren et al., 2003; Packer and Yuste, 2011), inhibition is most often studied as a local process. This has left a critical void in our understanding of how inhibition is distributed across large-scale networks. For example, thalamocortical projections are known to generate feedforward inhibition of pyramidal cells at their site of termination (Cruikshank et al., 2007; Porter et al., 2001). However, the inhibitory effects of thalamic input on regions downstream from their projection site remain unclear. We discovered that thalamic input to VLO drives robust inhibitory effects in downstream regions, including the contralateral hemisphere. To the best of our knowledge, this has not been shown before for any cortical region.

By pairing inactivation of zona incerta with electrophysiology, we found that stimulus-evoked inhibition in at least one cortical region is dependent on normal incertal processing. Future studies may combine incertal suppression with fMRI to assess whether ZI mediates inhibition throughout cortex. Previously, our group found that ZI inactivation reduced the degree of inhibition evoked in sensory cortex during 10 Hz stimulation of central thalamus (Liu et al., 2015). An important difference between these two studies is the spatial extent of inhibition. Unlike the widespread inhibition reported here, the negative fMRI signals driven by central thalamus stimulation were strictly localized to sensory cortex. This difference may be due to ZI's topographic organization. Anterograde studies have shown that the density of incertocortical terminals is strongest in sensory cortex (Lin et al., 1997). Furthermore, in our previous study, the thalamic projections that putatively drove incertal activity terminated in the dorsolateral ZI (Liu et al., 2015) – the same subregion of ZI that exhibits GABAergic projections to sensory cortex (Lin et al., 1990). The widespread nature of inhibition observed here suggests a broader activation of zona incerta covering multiple topographically organized subregions, perhaps supported by the extensive interconnections within ZI (Power and Mitrofanis, 1999). Future studies may wish to investigate the effect of stimulating ZI directly and/or the projections from VLO or thalamus to zona incerta.

Our proposal that zona incerta is responsible for the widespread inhibition evoked during 10 Hz stimulation of VLO afferents is consistent with previous characterizations of this region. The majority of incerto-cortical projections terminate in layer I, which is thought to provide diffuse inhibition over distal dendrites of cortical projection neurons (Lin et al., 1997). With extensive bilateral interconnections (Power and Mitrofanis, 1999, 2001; Shammah-Lagnado et al., 1985), the zona incerta is well situated to influence activity on both sides of the brain. This may explain why 10 Hz evoked a bilateral negative response, but 40 Hz stimulation had minimal influence on the contralateral hemisphere. Finally, paired electrophysiological recordings in cortex and zona incerta support the latter's role in frequency-dependent inhibition. One study found that rhythmically firing ZI units were synchronized to cortical firing during slow 1–4 Hz cortical waves (Bartho et al., 2007). Cortical oscillations in the 5–9 Hz range also exerted robust influence on ZI activity, but when cortex was dominated by fast oscillations in the beta and gamma range, there was no apparent relationship between incertal firing and cortical activity. The study's authors propose that incertal neurons exhibit frequency-dependent resonant properties or that different oscillatory patterns activate distinct cortico-incertal projections. A similar mechanism may explain our finding that widespread inhibition is evoked during low-, but not high-, frequency thalamocortical stimulation.

It is worth considering alternative mechanisms for the widespread inhibition evoked throughout cortex. Thalamic input to VLO might recruit nearby GABAergic projection neurons within cortex (Tamamaki and Tomioka, 2010). However, this population preferentially receives input from within cortex, and there is currently no evidence suggesting that thalamic projections would recruit such neurons (Tomioka et al., 2005). Downstream inhibition might also occur via cortico-cortical feedforward inhibition. It is well documented that spiking in cortical excitatory neurons can suppress nearby principal neurons via GABAergic interneurons in a frequency-dependent manner (Berger et al., 2009; Silberberg and Markram, 2007). Unlike our findings though, these studies show that high frequencies of stimulation generate the strongest inhibitory response. The use of slice preparations to characterize this phenomenon also makes it difficult to generalize such behavior to long-range connections.

Functional role of orbital networks

The VLO takes part in a negative feedback loop responsible for descending pain modulation via the midbrain and spinal cord (Tang et al., 2009). It represents affective or arousing aspects of pain (Follett and Dirks, 1995; Snow et al., 1992b), and imaging studies indicate that it supports arousal (Englot et al., 2009a). Our results build upon these studies by showing that thalamic input to VLO is capable of dynamically controlling forebrain activation and deactivation, which reflect states of heightened and reduced arousal, respectively. Pain signals transmitted through VLO may follow two pathways – one descending through the canonical midbrain-spinal cord pathway and one within forebrain via striatum, thalamus, cortex, and zona incerta. This view is supported by previously proposed roles for ZI in “linking diverse sensory channels to appropriate visceral, arousal, attention and posture-locomotion responses” (Mitrofanis, 2005). The frequency-dependent polarity of cortical responses suggests that thalamic input to VLO can both facilitate and suppress these behavioral responses. It has been hypothesized that OFC suppresses neuronal activity associated with aversive or painful sensations (Hooker and Knight, 2006). Our data confirm that OFC networks support the transformation of ascending thalamocortical signals to downstream inhibition. For example, neurons within the submedial nucleus fire within the 5–10 Hz frequency range in response to noxious stimuli (Kawakita et al., 1993), consistent with our finding that stimulating submedial projections in this range selectively drives cortical inhibition. Future experiments may investigate whether other VLO afferents (e.g. those from somatosensory cortex) also capable of eliciting widespread inhibition.

Beyond inhibition, our results link anatomical and physiological studies on orbitofrontal networks to quantitative measurements of downstream activation. Both low and high frequencies of thalamocortical stimulation within VLO drove robust activation of the ipsilateral striatum. This activation could be mediated by striatal collaterals of the stimulated projection (Kuramoto et al., 2017), or poly-synaptically via projections from orbitofrontal cortex to striatum. Until recently, this latter pathway had been relatively overlooked. However, accumulating evidence indicates a mediolateral topographic projection from the various sectors of orbital cortex to the caudate-putamen (Schilman et al., 2008). Tracing studies show that projections from VLO terminate centrally in the caudate-putamen. This pathway may allow sensory information ascending through VLO to interact with prelimbic and cingulate networks that converge on the same striatal region (Groenewegen and Uylings, 2010). Our fMRI data supports this approximate mapping, with low-frequency thalamocortical stimulation in VLO driving activation of the medial to central striatum. At higher frequencies of stimulation, activations covered almost all of striatum, suggesting the recruitment of local striatal circuits or other cortico-striatal pathways.

Implications for deep brain stimulation (DBS)

Deep brain stimulation within OFC has been explored as potential treatment for neurological disorders, but with mixed success (Klanker et al., 2013; Nauczyciel et al., 2014; Ruffini et al., 2009). Our work makes two contributions here. First, we show that stimulations of VLO can drive completely opposite effects throughout cortex, depending on the precise frequency used. Frequency is often a key parameter in optimizing the efficacy of DBS, and our study illustrates this with dramatic effect. Second, we show that stimulating different neuronal elements within the VLO circuit can elicit distinct responses across the brain. One limitation of DBS is that it cannot separately modulate different neuronal elements within a region. This makes it difficult to identify exact mechanisms of different DBS paradigms. By using optogenetics to selectively stimulate thalamocortical projections, thalamic relay neurons, and cortical projection neurons, we found that each element drives unique brain-wide responses. Future studies interested in therapeutic applications of OFC stimulation may wish to investigate particular elements within this circuit.

Significance for neurovascular coupling

Extracellular recordings were performed in this study to confirm that fMRI signals reflect underlying neuronal activity. They also offer important insight into the nature of neurovascular coupling, which remains an active area of research (Airaksinen et al., 2012; Huttunen et al., 2008; Kleinfeld et al., 2011; Uhlirova et al., 2016). Early studies on neurovascular coupling suggested that positive blood oxygen-level dependent (BOLD) signals reflect increases in synaptic input (Berens et al., 2012; Logothetis, 2003). However, others have shown a clear link between BOLD and spiking output (Lee et al., 2016; Liu et al., 2015). For example, various ofMRI studies have demonstrated that spiking elicits a local positive BOLD response (Domingos et al., 2011; Lee et al., 2016; Lee et al., 2010).

We found that the frequency-dependent responses measured with CBV-weighted fMRI – both positive and negative – reflect corresponding changes in neuronal firing rate (we refer to CBV polarity as the polarity after inverting the raw time series, so that a positive signal reflects increases in CBV, and vice versa). Especially noteworthy is that negative CBV signals were linked to neuronal inhibition. The neuronal interpretation of negative fMRI signals can be complex, given the variety of possible causes for regional inhibition and their different metabolic demands (Kim et al., 2014; Logothetis, 2008). Negative CBV and BOLD signals have both been linked to increases in neuronal spiking and LFP (Englot et al., 2008; Mishra et al., 2011; Schridde et al., 2008; Shih et al., 2009), and more recent studies have reported instances where decreases in cortical CBV are not associated with any changes in activity (Hu and Huang, 2015; Ma et al., 2017). Nevertheless, many studies have found that negative BOLD signals correspond to decreases in local firing rate (Englot et al., 2008; Lee et al., 2016; Liu et al., 2015; Shmuel et al., 2006). Our results support such findings and extend them to CBV, which is becoming increasingly common in preclinical fMRI studies.

STAR METHODS

Lead Contact and Materials Availability

Lead Contact—The study's Lead Contact is Jin Hyung Lee, PhD (ljinhy@stanford.edu). Correspondence can be made to 318 Campus Drive, #W300A; Stanford, CA 94305.

Materials Availability Statement—This study did not generate any new unique plasmids, mouse lines, or reagents.

Experimental Model and Subject Details

Animals—Healthy female Sprague-Dawley rats (12–14 weeks old at injection; Charles River, Wilmington, MA, RRID:RGD_734476) were used for all experiments. The average age of animals was 42 and 45 weeks for fMRI scanning and electrophysiology, respectively. Animals were not used previously in any other procedures. Animals were group-housed prior to surgery and individually housed after surgery under a 12 hour light-dark cycle. Animals were provided with food and water *ad libitum*. Animal husbandry and experimental manipulation were performed in strict accordance with National Institute of Health and Stanford University Institutional Animal Care and Use Committee (IACUC) guidelines.

Method Details

Viral Injections and Fiber Placement—Injections were performed with concentrated rAAV5-CaMKII-hChR2(H134R)-EYFP virus produced at the University of North Carolina vector core (8.5×10^{12} titer, lot #AV4316LM). During the injection procedure, rats were anesthetized with 2% isoflurane (Sigma-Aldrich, MO, USA) and secured in a stereotactic frame. Body temperature was maintained at 37 °C using a thermoresistive heating pad (FHC, Inc., ME, USA). Standard procedures for sterile surgery were followed. To prevent desiccation, artificial tears were applied to the eyes. After shaving the head, a triple scrub of 70% ethanol alternated with Betadine was applied. 200 µL of 0.5% bupivacaine was injected under the scalp. Slow-release buprenorphine was administered subcutaneously to minimize post-operative discomfort. Following a midline scalp incision, small craniotomies were performed with a dental drill above the submedial nucleus (−2.4 mm AP, +0.7 mm ML, −6.5 mm DV) and/or ventrolateral orbital cortex (+4.7 mm AP, +1.8 mm ML, −4.3 mm DV). Two microliters of virus were injected to the target region through a 10 mm 33 gauge beveled NanoFil needle (World Precision Instruments Inc., FL, USA) with a Micro4 microsyringe pump controller. For halorhodopsin experiments, 500 nL of rAAV5-hSyn-eNpHR3.0-mCherry-WPRE virus were injected into the right zona incerta after completion of the ChR2 injection (−3.96 mm AP, +2.8 mm ML, +7.4 mm DV; 6.7×10^{12} titer, lot #AV4834B from University of North Carolina at Chapel Hill vector core). Following completion of injection(s), custom-made 200 µm diameter fiber-optic implants (Thorlabs, Inc., NJ, USA, #FT200EMT; (Duffy et al., 2015)) were inserted and mounted to the skull using Clearfil AP-X light-cured dental cement (Kuraray Noritake Dental Inc., Japan, #1721-KA). This step was skipped in animals used for electrophysiology at the site of stimulation to allow for recording with an acute optrode. After suturing the incision, antiseptic Dermachlor rinse (Henry Schein, NY, USA) and 2% lidocaine hydrochloride jelly

(Akorn Pharmaceuticals, IL, USA) were topically applied. Animals were kept on a heating pad until recovery from anesthesia.

Optogenetic Functional MRI Data Acquisition—fMRI was performed in a 7T Bruker BioSpec small animal MRI system at Stanford University equipped with an 86 mm inner diameter transmit volume coil and a 2 cm inner diameter single-loop receive surface coil. Animals were initially anesthetized with 3–4% isoflurane and injected with 15 mg/kg of the contrast agent Feraheme (AMAG Pharmaceuticals, Inc., MA, USA) via tail vein before being secured in the MRI cradle. A 200 μm diameter optical fiber was connected to a 473 nm laser source (LaserGlow Technologies, Toronto, Canada) and coupled with the fiber-optic implant. A single ofMRI scan consisted of a block design with 30 s of baseline measurements followed by six 20 s pulse trains of light delivered once per minute over 6 minutes. For the primary comparison of 10 versus 40 Hz stimulation (Figures 1 and S3), 4–7 scans were typically collected per frequency for each animal in a single session. For secondary frequency sweep experiments (Figure 2), 1–3 scans were collected for each frequency. For control experiments in Figure S4, 7–9 scans were collected for each frequency. With the exception of control experiments presented in Figure S4, a duty cycle of 30% was used across frequencies to maintain the total amount of light delivery. Stimulation frequencies were randomized across imaging sessions. Optical power was calibrated to 5 mW at the implanted fiber's tip. In two of the animals used for Figure S4, a higher power level was used (no more than ~2x) to account for fibers implanted in a relatively dorsal position in VLO.

During fMRI scanning, animals were anesthetized with a mixture of O_2 (35%), N_2O (65%), and isoflurane (~1.5%). To ensure stable fMRI signals, body temperature was maintained at 37 °C using heated airflow. T2-weighted high-resolution anatomical images were acquired with a fast spin echo (RARE) sequence prior to fMRI scanning to check for brain damage and validate the optical fiber's location [$0.14\times0.14\times0.5$ mm^3 spatial resolution, 256×256 matrix size, 2500 ms TR, 33 ms TE, 30 slices, 90° flip angle] (Figure S1D). A spiral sequence was used to acquire fMRI images during photostimulation with the following parameters: 35×35 mm^2 in-plane field of view, $0.5\times0.5\times0.5$ mm^3 spatial resolution, 4 interleaves, 30° flip angle, 750 ms TR, 12 ms echo time, and 23 slices (Figure 1B). For some experiments, additional slices were acquired to facilitate image registration. Images were zero-padded in k-space to a 128×128 matrix size. Motion correction was performed using a GPU-based inverse Gauss-Newton algorithm to optimize detection of evoked responses (Fang and Lee, 2013). Scans with significant motion, identified by careful visual inspection for spiral artifacts and activations at the boundary of the brain, were excluded from analysis. Fewer than 2% of collected scans were excluded for this reason. Given that animals are anesthetized during imaging, these artifacts are likely due to occasional large breaths that distort the magnetic field.

In vivo Electrophysiology—*In vivo* electrophysiology was performed to directly measure the neuronal activity of various brain regions during thalamocortical stimulation. As with imaging, anesthesia was maintained with a mixture of O_2 (35%), N_2O (65%), and ~1.5% isoflurane. Throughout the procedure, body temperature was maintained at 37 °C using a thermoresistive heating pad (FHC, Inc., ME, USA). After securing the animal within a stereotactic frame, a 16-channel microelectrode array (NeuroNexus Technologies, MI, USA; A1×16 standard model linear electrode array) was inserted at the desired recording site. For recordings at the site of stimulation and zona incerta, an optical fiber glued to the electrode tip was used to deliver light. Remote recordings were performed at the following coordinates, averaged across animals: contralateral VLO (+4.68 mm AP, −1.90 mm ML, −4.90 mm DV), ipsilateral motor cortex (+3.24 mm AP, +2.43 mm ML, −3.00 mm DV), ipsilateral reticular nucleus (−1.86 mm AP, +2.20 mm ML, −6.93 mm DV), contralateral reticular nucleus (−1.92 mm AP, −2.10 mm ML, −7.17 mm DV), and ipsilateral zona incerta (−4.00 mm AP, +3.10 mm ML, −7.13 mm DV). Light was delivered to the fiber-optic implant at VLO via a 473 nm laser source calibrated to 5 mW power delivery. In one animal, a higher power level was used (no more than ~2x) to account for a fiber implanted in a relatively dorsal position in VLO. For the optrode positioned in zona incerta, a 200 μm diameter optical fiber was used to deliver continuous light from a 589 nm laser source (LaserGlow Technologies) calibrated to 5 mW at the implanted fiber's tip. Recordings were performed for 20 s without stimulation, followed by repeated stimulation cycles (20 s on, 40 s off) at 10 or 40 Hz with a 30% duty cycle. To assess the role of zona incerta, 10 Hz stimulation trials were interleaved with 30 s periods of simultaneous eNpHR activation beginning 5 s prior to 10 Hz stimulation (Figure 7B).

Intracerebral Infusions—Pharmacological infusions were performed during *in vivo* electrophysiology (same procedure as described above) with bicuculline methiodide (BMI; 0.6 mg/ml; Sigma-Aldrich #14343), lidocaine hydrochloride (2%; Fresenius Kabi, IL, USA; #491507), or sterile saline as a control. Solutions were delivered at a rate of 250 nL/min via two polyethylene cannulas (0.011/0.024" ID/OD; A-M Systems, WA, USA) – one for saline and one for the active pharmacological agent – glued to the tip of a recording electrode, directly above the topmost recording contact. Cannula tips were beveled to ensure that injected solutions were released in the direction of the electrode.

Infusions of saline and BMI (500 nL) were performed in the contralateral VLO while recording directly below the site of infusion (Figure 5B). For each solution, twenty 10 Hz stimulation/recording trials were performed before infusion onset, and twenty more trials were performed immediately after infusion. Saline was delivered first, followed by BMI. To assess the role of zona incerta, saline and lidocaine (500–1000 nL) were delivered to the ipsilateral zona incerta while recording in the contralateral VLO. Twenty 10 Hz stimulation/recording trials were performed before any infusion onset, followed by saline infusion, twenty stimulation/recording trials, lidocaine infusion, and another twenty stimulation/recording trials.

Immunohistochemistry—Standard immunohistochemistry techniques were used to amplify the endogenous EYFP signal fused to ChR2. Rats were deeply anesthetized with isoflurane and transcardially perfused with 0.1M phosphate-buffered saline (PBS) and ice-cold 4% paraformaldehyde (PFA) in PBS. Brains were extracted and fixed in 4% PFA overnight at 4 °C. Brains were then equilibrated in 30% sucrose in PBS at 4 °C. Coronal sections (40 μm) were prepared on a freezing microtome. Free-floating sections were: [1]

washed 5 times with PBS (10 mins each), [2] blocked and permeabilized with 5% normal donkey serum (NDS) and 0.4% Triton X-100 in PBS for 1 hr, [3] incubated at 4 °C overnight with primary antibody against chicken green fluorescent protein (1:1000; Aves, OR, USA; #GFP-1020, RRID:AB_2307313), [4] washed 7 times with a 2% NDS in PBS wash buffer (10 mins each), [5] incubated for 1 hr at room temperature with the secondary antibody Alexa Fluor 568 goat anti-chicken IgY (1:500; Thermo Fisher Scientific, MA, USA; #A-11041, RRID:AB_2534098), [6] washed 7 times with the wash buffer (10 mins each), [7] washed 2 times with PBS (20 mins each), [8] incubated with DAPI (0.002% DAPI [5 mg/ml] in PBS; Thermo Fisher Scientific, #D1306, RRID:AB_2629482) for 5 minutes, [9] washed 3 times with PBS (10 mins each), and [10] mounted with Fluoromount-G (SouthernBiotech, AL, USA; #0100-01). Immuno-fluorescence was assessed with a Zeiss laser confocal microscope. Antibodies were diluted with a solution of 5% NDS and 0.1% Tween-20 in PBS.

Quantification and Statistical Analysis

Functional MRI Data Analysis—fMRI data processing was performed with SPM12 (Ashburner et al., 2014) in Matlab (MathWorks, Inc., MA, USA). Motion-corrected images belonging to the same stimulation frequency and scanning session were first spatially smoothed (0.4 mm FWHM Gaussian kernel) and averaged together. The average 4D images were then aligned to a common coordinate frame using affine and non-rigid transformations with NiftyReg (Modat et al., 2014; Modat et al., 2010). Within each animal, an equal number of scans for each frequency were averaged together. For the frequency sweep experiments, one animal lacked 15 Hz data and another lacked 25 and 30 Hz data.

Fixed effect analyses were performed at the subject level using a general linear model. The design matrix (Figure 1C) was created by convolving the stimulation paradigm with fourth-order gamma basis functions, which have been shown to be optimal for balancing detection and characterization of heterogeneous fMRI signals (Liu et al., 2017). For quantification of active brain volume at the single-subject level, active voxels were identified as those with a t-score magnitude greater than 3.16 ($p < 0.001$, uncorrected). Fixed effect analyses were also performed at the group level to generate the activation maps in Figures 1–3. Voxels with a t-statistic magnitude corresponding to significant p-values were overlaid onto a T2-weighted anatomical image averaged across subjects. Warm colors in activation maps indicate positive t-scores, while cool colors indicate negative t-scores. Regions of interest visualized in Figure S3A were defined by matching a superimposed digital rat brain atlas (Paxinos and Watson, 2006) to visible anatomical features.

Time series were calculated on a voxel-wise basis from each animal's average 4D image as the percent modulation of the fMRI signal relative to the 30 s baseline period collected prior to stimulation. Detrending was performed with a 1 minute moving average kernel. With the exception of Figure S2, which averaged over significantly modulated voxels only, time series were generated by averaging across animals the mean time series of all voxels in the corresponding region of interest. To better compare responses across frequencies in Figure 2, time series were vertically shifted to start at 0% change. The percent signal change calculated from the raw fMRI signal was also inverted in order to make increases in signal portray increases in CBV. ∑fMRI values in Figures S3 and S4 were calculated at the sum of the fMRI response over all measured time points, excluding the 30 s baseline period collected before the first stimulation cycle (120 points over six minutes, in total) (Lee et al., 2016).

Electrophysiology Analysis—Recordings were performed with either the OpenEphys recording system and GUI (Siegle et al., 2017) or Plexon OmniPlex system with PlexControl software (Plexon Inc., TX, USA). For the OpenEphys recordings, signals were collected at 30 kHz and band-pass filtered between 300 Hz and 6 kHz. Spike detection and clustering were performed with the *Wave_Clus* software package in Matlab, using wavelets and super-paramagnetic clustering (Quiroga et al., 2004). For recordings made with the Plexon system, the Plexon multichannel acquisition processor was used to amplify and band-pass filter the acquired signal between 150 Hz and 8 kHz. Signals were digitized at 40 kHz and processed to extract action potentials in real-time.

Statistics—Statistical tests were performed in Matlab. Exact values of N for all tests can be found in the main text, figures, and figure legends. For volumetric comparisons in Figure S3, two-tailed paired t-tests were used to identify changes in the amount of fMRI activation between 10 and 40 Hz. For comparisons of ∑fMRI against zero in Figure S3, two-tailed t-tests were applied. For *in vivo* electrophysiology, two-tailed paired t-tests were used to identify significant changes in firing rate within each unit between pre-stimulation and stimulation periods. For experiments with ChR2 stimulation only, these periods were 20 s each. For experiments with only eNpHR activation, the 30 s eNpHR period was compared with the 15 s pre-stimulus period. For experiments with both ChR2 stimulation and eNpHR activation, the 20 s ChR2 period was compared with the 15 s period before either stimulus was delivered. Independence was assumed between repeated electrophysiology trials. Histograms of percent changes in firing rate (Figures 4, 5, 7 and S6) were compared using a two-tailed Mann-Whitney U-test across units since assumptions on normality could not be met. Histograms in Figure 6 were compared using a one-way non-parametric ANOVA test (i.e. Kruskal-Wallis) with Tukey-Kramer post-hoc comparisons. For all histogram comparisons, data for each unit was obtained by averaging over repeated trials, and single-units were assumed to represent independent samples. Baseline firing rates in Figure 5 were compared using a two-tailed t-test for individual units and a two-tailed paired t-test across all units. For all tests, variance was generally similar across groups being compared and significance was determined at the $\alpha = 0.05$ cutoff level.

Data and Code Availability

Requests for raw data should be directed to and will be fulfilled by the Lead Contact, Jin Hyung Lee (ljinhy@stanford.edu), Stanford University.

Supplementary Material

Refer to Web version on PubMed Central for supplementary material.

ACKNOWLEDGEMENTS

This work was supported by NIH/NINDS R01NS087159, NIH/NIA R01NS091461, NIH/NINDS RF1AG047666, and NIH/NIMH RF1MH114227. The authors thank Florian Schmid for help acquiring high-resolution *ex vivo* images.

REFERENCES

Airaksinen AM, Hekmatyar SK, Jerome N, Niskanen JP, Huttunen JK, Pitkänen A, Kauppinen RA, and Gröhn OH (2012). Simultaneous BOLD fMRI and local field potential measurements during kainic acid–induced seizures. Epilepsia 53, 1245–1253. [PubMed: 22690801]

Alcaraz F, Marchand AR, Vidal E, Guillou A, Faugère A, Coutureau E, and Wolff M (2015). Flexible use of predictive cues beyond the orbitofrontal cortex: role of the submedius thalamic nucleus. J Neurosci 35, 13183–13193. [PubMed: 26400947]

Ashburner J, Barnes G, Chen C, Daunizeau J, Flandin G, Friston K, Kiebel S, Kilner J, Litvak V, and Moran R (2014). SPM12 manual. Wellcome Trust Centre for Neuroimaging, London, UK.

Backonja M, and Miletic V (1991). Responses of neurons in the rat ventrolateral orbital cortex to phasic and tonic nociceptive stimulation. Brain Res 557, 353–355. [PubMed: 1747767]

Bartho P, Slezia A, Varga V, Bokor H, Pinault D, Buzsaki G, and Acsady L (2007). Cortical control of zona incerta. J Neurosci 27, 1670–1681. [PubMed: 17301175]

Bedwell SA, Billett EE, Crofts JJ, and Tinsley CJ (2014). The topology of connections between rat prefrontal, motor and sensory cortices. Frontiers in systems neuroscience 8, 177. [PubMed: 25278850]

Berens P, Logothetis NK, and Tolias AS (2012). Local Field Potentials, BOLD, and Spiking Activity: Relationships and Physiological Mechanisms. Comput Neurosci-Mit, 599–623.

Berger TK, Perin R, Silberberg G, and Markram H (2009). Frequency-dependent disynaptic inhibition in the pyramidal network: a ubiquitous pathway in the developing rat neocortex. The Journal of physiology 587, 5411–5425. [PubMed: 19770187]

Chen Y, Wang H, Zhang R, Wang H, Peng Z, Sun R, and Tan Q (2012). Microinjection of sanguinarine into the ventrolateral orbital cortex inhibits Mkp-1 and exerts an antidepressant-like effect in rats. Neurosci Lett 506, 327–331. [PubMed: 22155096]

Coffield J, Bowen K, and Miletic V (1992). Retrograde tracing of projections between the nucleus submedius, the ventrolateral orbital cortex, and the midbrain in the rat. Journal of Comparative Neurology 321, 488–499.

Corwin JV, Fussinger M, Meyer RC, King VR, and Reep RL (1994). Bilateral destruction of the ventrolateral orbital cortex produces allocentric but not egocentric spatial deficits in rats. Behavioural brain research 61, 79–86. [PubMed: 8031498]

Craig A Jr, Wiegand S, and Price J (1982). The thalamo - cortical projection of the nucleus submedius in the cat. Journal of Comparative Neurology 206, 28–48.

Cruikshank SJ, Lewis TJ, and Connors BW (2007). Synaptic basis for intense thalamocortical activation of feedforward inhibitory cells in neocortex. Nature neuroscience 10, 462–468. [PubMed: 17334362]

Domingos AI, Vaynshteyn J, Voss HU, Ren XY, Gradinaru V, Zang F, Deisseroth K, de Araujo IE, and Friedman J (2011). Leptin regulates the reward value of nutrient. Nature neuroscience 14, 1562–U1592. [PubMed: 22081158]

Duffy BA, Choy M, Chuapoco MR, Madsen M, and Lee JH (2015). MRI compatible optrodes for simultaneous LFP and optogenetic fMRI investigation of seizure-like afterdischarges. NeuroImage 123, 173–184. [PubMed: 26208873]

Englot DJ, Mishra AM, Mansuripur PK, Herman P, Hyder F, and Blumenfeld H (2008). Remote effects of focal hippocampal seizures on the rat neocortex. J Neurosci 28, 9066–9081. [PubMed: 18768701]

Englot DJ, Modi B, Mishra AM, DeSalvo M, Hyder F, and Blumenfeld H (2009a). Cortical deactivation induced by subcortical network dysfunction in limbic seizures. J Neurosci 29, 13006–13018. [PubMed: 19828814]

Englot DJ, Modi B, Mishra AM, DeSalvo M, Hyder F, and Blumenfeld H (2009b). Cortical deactivation induced by subcortical network dysfunction in limbic seizures. J Neurosci 29, 13006–13018. [PubMed: 19828814]

Eshel N, Nelson EE, Blair RJ, Pine DS, and Ernst M (2007). Neural substrates of choice selection in adults and adolescents: development of the ventrolateral prefrontal and anterior cingulate cortices. Neuropsychologia 45, 1270–1279. [PubMed: 17118409]

Fang Z, and Lee JH (2013). High-throughput optogenetic functional magnetic resonance imaging with parallel computations. Journal of neuroscience methods 218, 184–195. [PubMed: 23747482]

Feierstein CE, Quirk MC, Uchida N, Sosulski DL, and Mainen ZF (2006). Representation of spatial goals in rat orbitofrontal cortex. Neuron 51, 495–507. [PubMed: 16908414]

Fino E, and Yuste R (2011). Dense inhibitory connectivity in neocortex. Neuron 69, 1188–1203. [PubMed: 21435562]

Follett KA, and Dirks B (1995). Responses of neurons in ventrolateral orbital cortex to noxious visceral stimulation in the rat. Brain Res 669, 157–162. [PubMed: 7712170]

Groenewegen H (1988). Organization of the afferent connections of the mediodorsal thalamic nucleus in the rat, related to the mediodorsal-prefrontal topography. Neuroscience 24, 379–431. [PubMed: 2452377]

Groenewegen HJ, and Uylings HB (2010). Organization of prefrontal-striatal connections. In Handbook of Behavioral Neuroscience (Elsevier), pp. 353–365.

Hardung S, Epple R, Jäckel Z, Eriksson D, Uran C, Senn V, Gibor L, Yizhar O, and Diester I (2017). A functional gradient in the rodent prefrontal cortex supports behavioral inhibition. Current Biology 27, 549–555. [PubMed: 28190729]

Holmgren C, Harkany T, Svennenfors B, and Zilberter Y (2003). Pyramidal cell communication within local networks in layer 2/3 of rat neocortex. The Journal of physiology 551, 139–153. [PubMed: 12813147]

Hooker CI, and Knight RT (2006). The role of lateral orbitofrontal cortex in the inhibitory control of emotion. In The orbitofrontal cortex, Zald D, and Rauch S, eds. (Oxford Univ. Press), pp. 307–324.

Hu D, and Huang L (2015). Negative hemodynamic response in the cortex: evidence opposing neuronal deactivation revealed via optical imaging and electrophysiological recording. J Neurophysiol 114, 2152–2161. [PubMed: 26180117]

Huang X, Tang J-S, Yuan B, and Jia H (2001). Morphine applied to the ventrolateral orbital cortex produces a naloxone-reversible antinociception in the rat. Neurosci Lett 299, 189–192. [PubMed: 11165767]

Huttunen JK, Gröhn O, and Penttonen M (2008). Coupling between simultaneously recorded BOLD response and neuronal activity in the rat somatosensory cortex. NeuroImage 39, 775–785. [PubMed: 17964186]

Isaacson JS, and Scanziani M (2011). How inhibition shapes cortical activity. Neuron 72, 231–243. [PubMed: 22017986]

Izquierdo A (2017). Functional heterogeneity within rat orbitofrontal cortex in reward learning and decision making. J Neurosci 37, 10529–10540. [PubMed: 29093055]

Kawakita K, Dostrovsky JO, Tang JS, and Chiang CY (1993). Responses of Neurons in the Rat Thalamic Nucleus Submedius to Cutaneous, Muscle and Visceral Nociceptive Stimuli. Pain 55, 327–338. [PubMed: 8121694]

Kim R, Hyder F, and Blumenfeld H (2014). Physiological basis of BOLD fMRI decreases. In Neurovascular Coupling Methods (Springer), pp. 221–236.

King V, Corwin J, and Reep R (1989). Production and characterization of neglect in rats with unilateral lesions of ventrolateral orbital cortex. Experimental neurology 105, 287–299. [PubMed: 2767200]

Klanker M, Post G, Joosten R, Feenstra M, and Denys D (2013). Deep brain stimulation in the lateral orbitofrontal cortex impairs spatial reversal learning. Behavioural brain research 245, 7–12. [PubMed: 23396148]

Kleinfeld D, Blinder P, Drew PJ, Driscoll JD, Muller A, Tsai PS, and Shih AY (2011). A guide to delineate the logic of neurovascular signaling in the brain. Frontiers in neuroenergetics 3, 1. [PubMed: 21559095]

Krettek J, and Price J (1977). The cortical projections of the mediodorsal nucleus and adjacent thalamic nuclei in the rat. Journal of Comparative Neurology 171, 157–191.

Kuramoto E, Iwai H, Yamanaka A, Ohno S, Seki H, Tanaka YR, Furuta T, Hioki H, and Goto T (2017). Dorsal and ventral parts of thalamic nucleus submedius project to different areas of rat orbitofrontal cortex: A single neuron-tracing study using virus vectors. The Journal of comparative neurology 525, 3821–3839. [PubMed: 28863230]

Lee HJ, Weitz AJ, Bernal-Casas D, Duffy BA, Choy M, Kravitz AV, Kreitzer AC, and Lee JH (2016). Activation of Direct and Indirect Pathway Medium Spiny Neurons Drives Distinct Brain-wide Responses. Neuron 91, 412–424. [PubMed: 27373834]

Lee JH, Durand R, Gradinaru V, Zhang F, Goshen I, Kim DS, Fenno LE, Ramakrishnan C, and Deisseroth K (2010). Global and local fMRI signals driven by neurons defined optogenetically by type and wiring. Nature 465, 788–792. [PubMed: 20473285]

Lewis LD, Voigts J, Flores FJ, Schmitt LI, Wilson MA, Halassa MM, and Brown EN (2015). Thalamic reticular nucleus induces fast and local modulation of arousal state. eLife 4, e08760. [PubMed: 26460547]

Lin CS, Nicolelis MAL, Schneider JS, and Chapin JK (1990). A Major Direct Gabaergic Pathway from Zona Incerta to Neocortex. Science 248, 1553–1556. [PubMed: 2360049]

Lin H, Geng X, Dang W, Wu B, Dai Z, Li Y, Yang Y, Zhang H, and Shi J (2012). Molecular mechanisms associated with the antidepressant effects of the class I histone deacetylase inhibitor MS-275 in the rat ventrolateral orbital cortex. Brain Res 1447, 119–125. [PubMed: 22341874]

Lin RC, Nicolelis MA, and Chapin JK (1997). Topographic and laminar organizations of the incertocortical pathway in rats. Neuroscience 81, 641–651. [PubMed: 9316017]

Liu J, Duffy BA, Bernal-Casas D, Fang Z, and Lee JH (2017). Comparison of fMRI analysis methods for heterogeneous BOLD responses in block design studies. NeuroImage 147, 390–408. [PubMed: 27993672]

Liu J, Lee HJ, Weitz AJ, Fang Z, Lin P, Choy M, Fisher R, Pinskiy V, Tolpygo A, Mitra P, et al. (2015). Frequency-selective control of cortical and subcortical networks by central thalamus. eLife 4, e09215. [PubMed: 26652162]

Logothetis NK (2003). The underpinnings of the BOLD functional magnetic resonance imaging signal. J Neurosci 23, 3963–3971. [PubMed: 12764080]

Logothetis NK (2008). What we can do and what we cannot do with fMRI. Nature 453, 869–878. [PubMed: 18548064]

Ma Z, Cao P, Sun P, Lu Z, Li L, Chen Y, and Chai X (2017). Negative hemodynamic response without neuronal inhibition investigated by combining optical imaging and electrophysiological recording. Neurosci Lett 637, 161–167. [PubMed: 27856222]

Mishra AM, Ellens DJ, Schridde U, Motelow JE, Purcaro MJ, DeSalvo MN, Enev M, Sanganahalli BG, Hyder F, and Blumenfeld H (2011). Where fMRI and electrophysiology agree to disagree: corticothalamic and striatal activity patterns in the WAG/Rij rat. J Neurosci 31, 15053–15064. [PubMed: 22016539]

Mitrofanis J (2005). Some certainty for the “zone of uncertainty”? Exploring the function of the zona incerta. Neuroscience 130, 1–15. [PubMed: 15561420]

Modat M, Cash DM, Daga P, Winston GP, Duncan JS, and Ourselin S (2014). Global image registration using a symmetric block-matching approach. Journal of medical imaging 1, 024003. [PubMed: 26158035]

Modat M, Ridgway GR, Taylor ZA, Lehmann M, Barnes J, Hawkes DJ, Fox NC, and Ourselin S (2010). Fast free-form deformation using graphics processing units. Computer methods and programs in biomedicine 98, 278–284. [PubMed: 19818524]

Nauczyciel C, Le Jeune F, Naudet F, Douabin S, Esquevin A, Vérin M, Dondaine T, Robert G, Drapier D, and Millet B (2014). Repetitive transcranial magnetic stimulation over the orbitofrontal cortex for obsessive-compulsive disorder: a double-blind, crossover study. Translational psychiatry 4, e436. [PubMed: 25203167]

Nicolelis MA, Chapin JK, and Lin RC (1992). Somatotopic maps within the zona incerta relay parallel GABAergic somatosensory pathways to the neocortex, superior colliculus, and brainstem. Brain Res 577, 134–141. [PubMed: 1521138]

Packer AM, and Yuste R (2011). Dense, unspecific connectivity of neocortical parvalbumin-positive interneurons: a canonical microcircuit for inhibition? J Neurosci 31, 13260–13271. [PubMed: 21917809]

Paxinos G, and Watson C (2006). The rat brain in stereotaxic coordinates: hard cover edition (Elsevier).

Pinault D (2004). The thalamic reticular nucleus: structure, function and concept. Brain Res Rev 46, 1–31. [PubMed: 15297152]

Porter JT, Johnson CK, and Agmon A (2001). Diverse types of interneurons generate thalamus-evoked feedforward inhibition in the mouse barrel cortex. J Neurosci 21, 2699–2710. [PubMed: 11306623]

Power BD, and Mitrofanis J (1999). Evidence for extensive inter-connections within the zona incerta in rats. Neurosci Lett 267, 9–12. [PubMed: 10400236]

Power BD, and Mitrofanis J (2001). Zona incerta: Substrate for contralateral interconnectivity in the thalamus of rats. The Journal of comparative neurology 436, 52–63. [PubMed: 11413546]

Price JL (2007). Definition of the orbital cortex in relation to specific connections with limbic and visceral structures and other cortical regions. Annals of the New York Academy of Sciences 1121, 54–71. [PubMed: 17698999]

Quiroga RQ, Nadasdy Z, and Ben-Shaul Y (2004). Unsupervised spike detection and sorting with wavelets and superparamagnetic clustering. Neural Comput 16, 1661–1687. [PubMed: 15228749]

Reep R, Corwin J, and King V (1996). Neuronal connections of orbital cortex in rats: topography of cortical and thalamic afferents. Exp Brain Res 111, 215–232. [PubMed: 8891652]

Ruffini C, Locatelli M, Lucca A, Benedetti F, Insacco C, and Smeraldi E (2009). Augmentation effect of repetitive transcranial magnetic stimulation over the orbitofrontal cortex in drug-resistant obsessive-compulsive disorder patients: a controlled investigation. Primary care companion to the Journal of clinical psychiatry 11, 226.

Schilman EA, Uylings HB, Galis-de Graaf Y, Joel D, and Groenewegen HJ (2008). The orbital cortex in rats topographically projects to central parts of the caudate-putamen complex. Neurosci Lett 432, 40–45. [PubMed: 18248891]

Schridde U, Khubchandani M, Motelow JE, Sanganahalli BG, Hyder F, and Blumenfeld H (2008). Negative BOLD with large increases in neuronal activity. Cerebral cortex 18, 1814–1827. [PubMed: 18063563]

Shammah-Lagnado SJ, Negrao N, and Ricardo JA (1985). Afferent connections of the zona incerta: a horseradish peroxidase study in the rat. Neuroscience 15, 109–134. [PubMed: 4010931]

Shih YY, Chen CC, Shyu BC, Lin ZJ, Chiang YC, Jaw FS, Chen YY, and Chang C (2009). A new scenario for negative functional magnetic resonance imaging signals: endogenous neurotransmission. J Neurosci 29, 3036–3044. [PubMed: 19279240]

Shmuel A, Augath M, Oeltermann A, and Logothetis NK (2006). Negative functional MRI response correlates with decreases in neuronal activity in monkey visual area V1. Nature neuroscience 9, 569–577. [PubMed: 16547508]

Siegle JH, Lopez AC, Patel YA, Abramov K, Ohayon S, and Voigts J (2017). Open Ephys: an open-source, plugin-based platform for multichannel electrophysiology. J Neural Eng 14.

Silberberg G, and Markram H (2007). Disynaptic inhibition between neocortical pyramidal cells mediated by Martinotti cells. Neuron 53, 735–746. [PubMed: 17329212]

Smith Y (2008). The thalamus. In Neuroscience in Medicine (Springer), pp. 419–442.

Snow P, Lumb B, and Cervero F (1992a). The representation of prolonged and intense, noxious somatic and visceral stimuli in the ventrolateral orbital cortex of the cat. Pain 48, 89–99. [PubMed: 1738579]

Snow PJ, Lumb BM, and Cervero F (1992b). The representation of prolonged and intense, noxious somatic and visceral stimuli in the ventrolateral orbital cortex of the cat. Pain 48, 89–99. [PubMed: 1738579]

Stalnaker TA, Cooch NK, and Schoenbaum G (2015). What the orbitofrontal cortex does not do. Nature neuroscience 18, 620. [PubMed: 25919962]

Tamamaki N, and Tomioka R (2010). Long-Range GABAergic Connections Distributed throughout the Neocortex and their Possible Function. Frontiers in neuroscience 4, 202. [PubMed: 21151790]

Tang JS, Qu CL, and Huo FQ (2009). The thalamic nucleus submedius and ventrolateral orbital cortex are involved in nociceptive modulation: A novel pain modulation pathway. Prog Neurobiol 89, 383–389. [PubMed: 19819292]

Tomioka R, Okamoto K, Furuta T, Fujiyama F, Iwasato T, Yanagawa Y, Obata K, Kaneko T, and Tamamaki N (2005). Demonstration of long-range GABAergic connections distributed throughout the mouse neocortex. The European journal of neuroscience 21, 1587–1600. [PubMed: 15845086]

Uhlirova H, Kilic K, Tian P, Thunemann M, Desjardins M, Saisan PA, Sakadzic S, Ness TV, Mateo C, Cheng Q, et al. (2016). Cell type specificity of neurovascular coupling in cerebral cortex. eLife 5.

Xing B, Zhao Y, Zhang H, Dang Y, Chen T, Huang J, and Luo Q (2011). Microinjection of valproic acid into the ventrolateral orbital cortex exerts an antidepressant-like effect in the rat forced swim test. Brain Res Bull 85, 153–157. [PubMed: 21419831]

Yoshida A, Dostrovsky JO, and Chiang CY (1992). The afferent and efferent connections of the nucleus submedius in the rat. The Journal of comparative neurology 324, 115–133. [PubMed: 1383287]

Zhang S, Tang J-S, Yuan B, and Jia H (1998). Inhibitory effects of electrical stimulation of ventrolateral orbital cortex on the rat jaw-opening reflex. Brain Res 813, 359–366. [PubMed: 9838193]

Zhang Y-Q, Tang J-S, Yuan B, and Jia H (1997). Inhibitory effects of electrically evoked activation of ventrolateral orbital cortex on the tail-flick reflex are mediated by periaqueductal gray in rats. Pain 72, 127–135. [PubMed: 9272796]

Zhao Y, Xing B, Dang Y.-h., Qu C.-l., Zhu F, and Yan C.-x. (2013). Microinjection of valproic acid into the ventrolateral orbital cortex enhances stress-related memory formation. Plos One 8, e52698. [PubMed: 23300985]

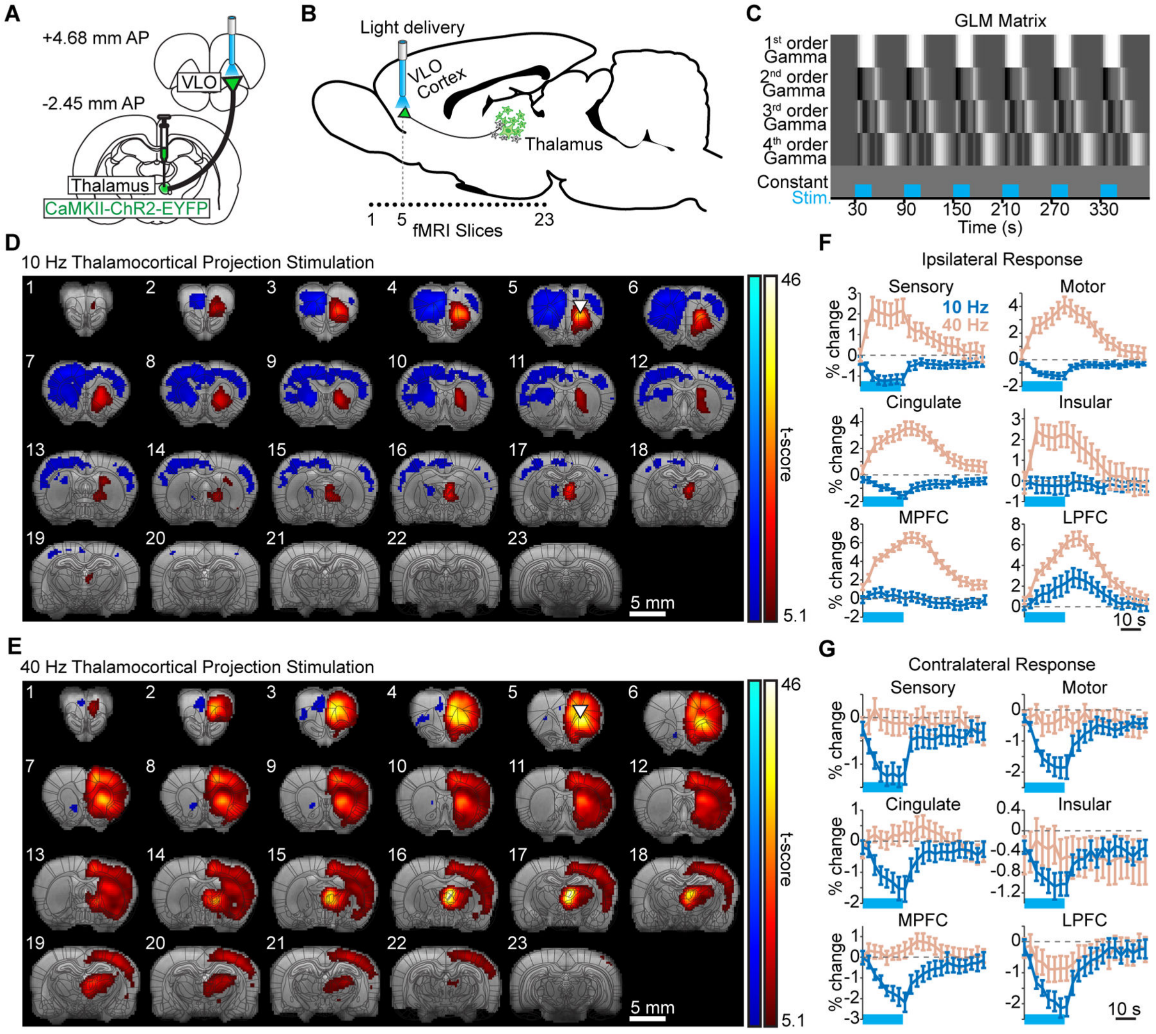

Figure 1. Optogenetic fMRI reveals robust but divergent responses to thalamocortical stimulation in VLO at 10 and 40 Hz.

(*A*) Experimental design for virus injection and thalamocortical stimulation. (*B*) Schematic of 23 coronal slices acquired in ofMRI experiments. (*C*) Design matrix for the block-design stimulation paradigm. (*D,E*) Group-level activation maps during thalamocortical stimulation at 10 (D) and 40 (E) Hz (N=11 animals; $p < 0.05$, FWE-corrected). In these and all other activation maps, white triangles indicate site of stimulation; warm colors indicate positive t-scores; cool colors indicate negative t-scores; image numbers correspond to slices shown in panel B. (*F,G*) Single-cycle fMRI time series from segmented areas of ipsilateral (F) and contralateral (G) cortex. Horizontal blue lines indicate the stimulation period. Error bars represent mean ± s.e.m. across animals (N=11). See also Figures S1–S4.

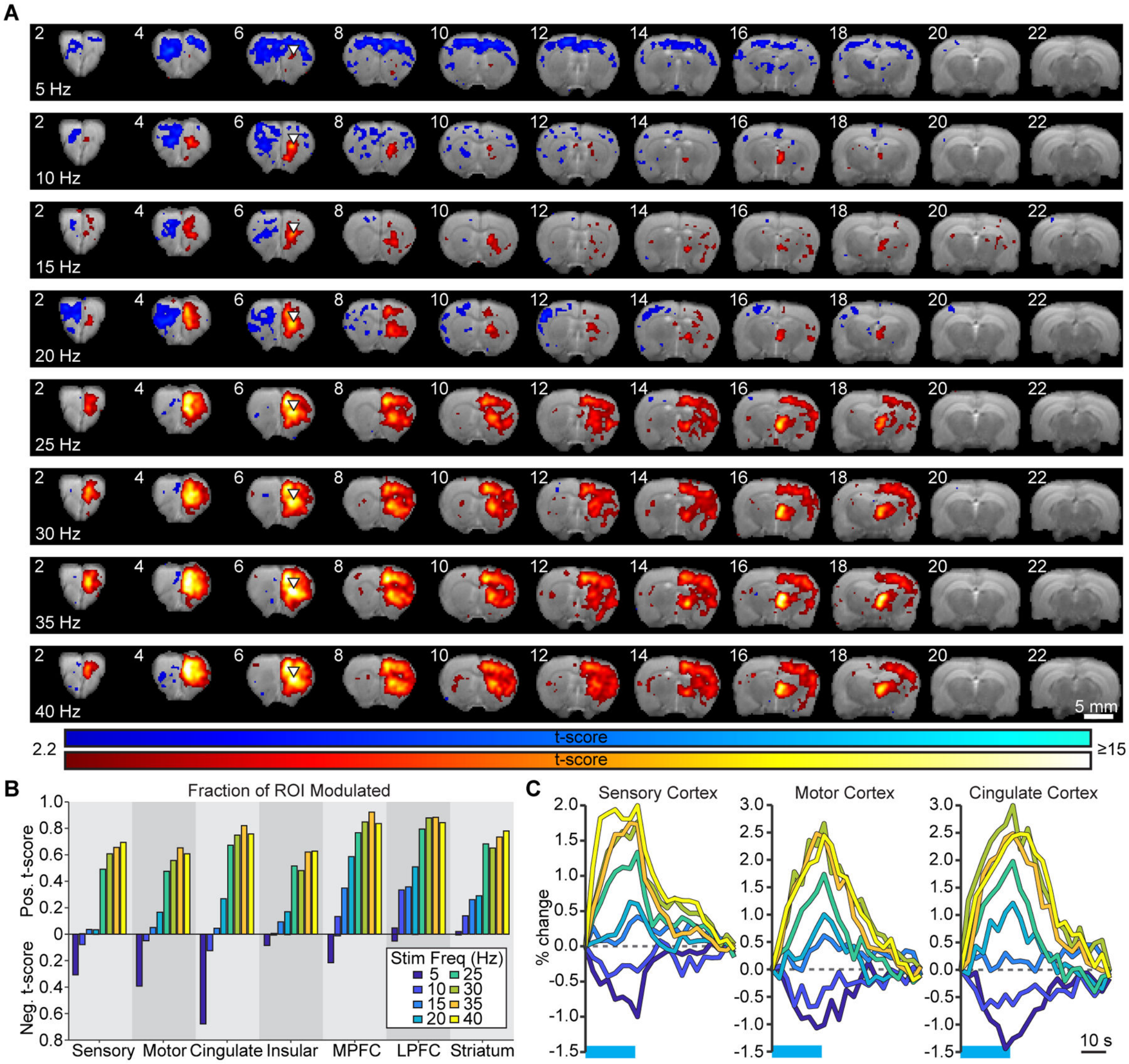

Figure 2. Frequency sweep experiments reveal transitions in evoked activity patterns between low and high stimulation frequencies.

(*A*) Group-level activation maps during thalamocortical stimulation in VLO at frequencies ranging from 5 to 40 Hz (N=7 animals; $p < 0.005$, uncorrected). (*B*) Quantification of significantly modulated brain volume in the ipsilateral hemisphere. Values represent the fraction of voxels within each ROI that are significantly modulated in group-level activation maps. (*C*) Average single-cycle time series illustrate the frequency-dependent transition from negative to positive responses in sensory, motor, and cingulate cortex. Horizontal blue lines indicate the stimulation period.

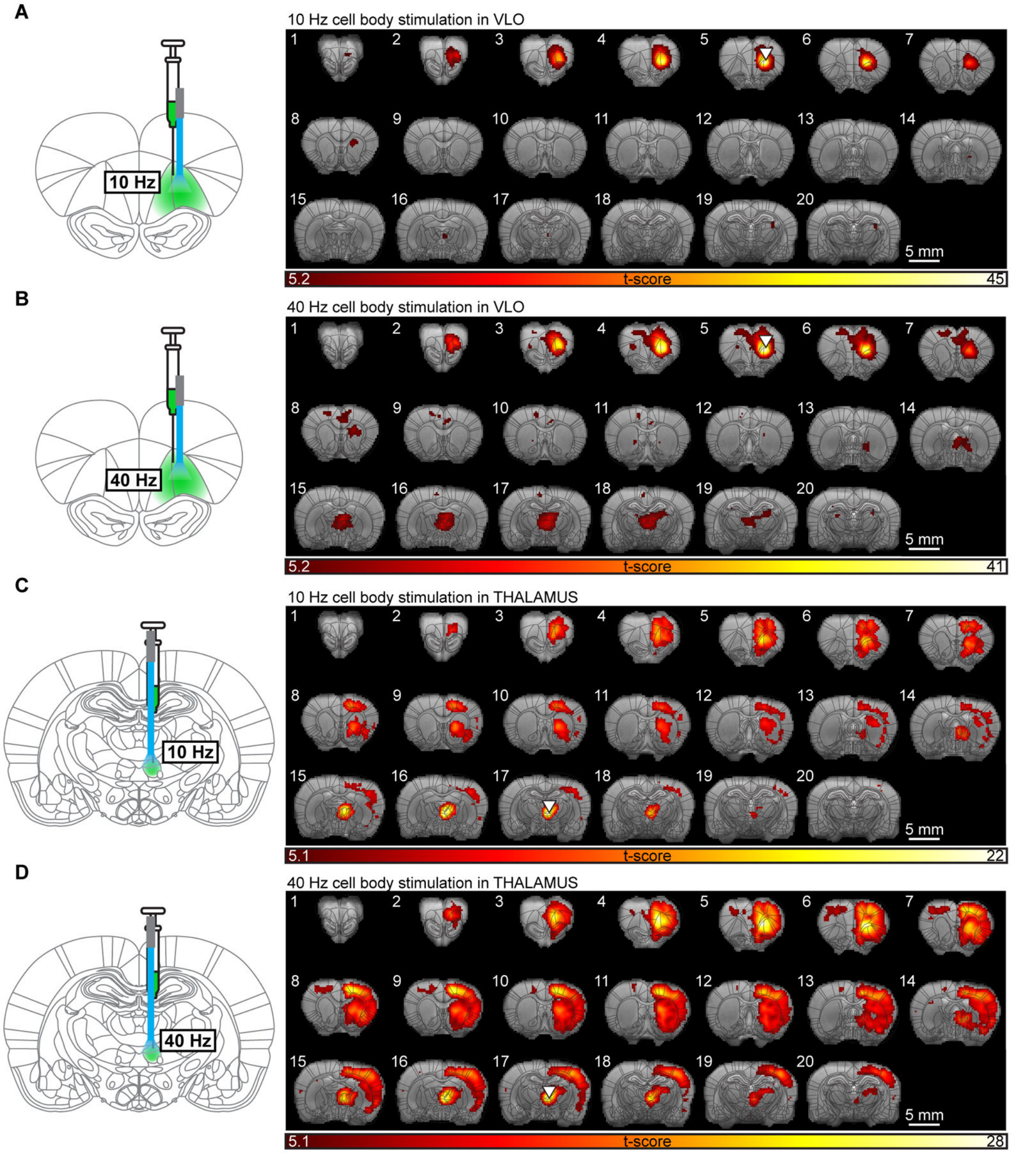

Figure 3. Widespread negative fMRI signals are not evoked during stimulation of cell bodies in VLO or thalamus.

(*A*,*B*) Group-level activation maps during stimulation of cell bodies in VLO at 10 (A) and 40 (B) Hz (N=5 animals; $p < 0.05$, FWE-corrected). (*C*,*D*) Group-level activation maps of evoked responses during stimulation of cell bodies in the submedial nucleus of thalamus at 10 (C) and 40 (D) Hz (N=5 animals; $p < 0.05$, FWE-corrected).

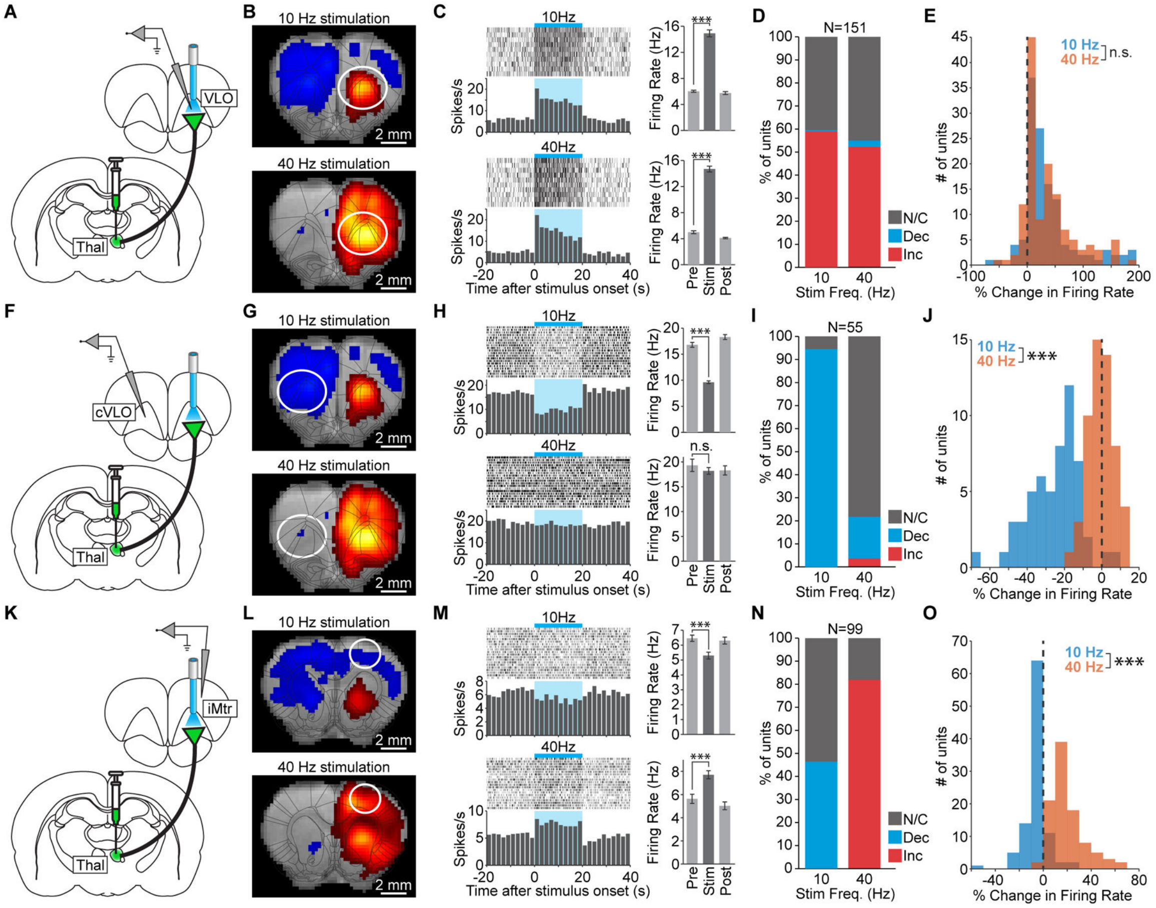

Figure 4. Electrophysiology corroborates frequency-dependent fMRI signals.

(*A*) Schematic of single-unit recordings at the site of stimulation in VLO. (*B*) 10 and 40 Hz stimulations drive robust positive fMRI signals at the site of stimulation. (*C*) Peri-event time histograms from a representative unit in VLO that is excited during 10 and 40 Hz stimulation ($p=1.2\times10^{-7}$ and 7.6×10^{-10}, respectively). Error bars represent mean ± s.e.m. over trials. (*D*) Quantification of significant changes in firing rate across recorded units. INC: increase, DEC: decrease, N/C: no change. (*E*) Histograms of stimulus-evoked changes in VLO firing rate (n.s. not significant; $p=0.38$). (*F*) Schematic of single-unit recordings in the contralateral VLO (cVLO). (*G*) 10 Hz stimulation drives a robust negative fMRI signal in cVLO that largely disappears during 40 Hz stimulation. (*H*) Peri-event time histograms from a representative unit in cVLO. The firing rate decreases during 10 Hz stimulation ($p=4.6\times10^{-13}$) but does not change during 40 Hz stimulation ($p=0.42$). (*I*) Quantification of significant changes in firing rate across recorded units in cVLO. (*J*) Histograms of stimulus-evoked changes in cVLO firing rate ($p=4.5\times10^{-17}$). (*K*) Schematic of single-unit recording in the ipsilateral motor cortex (iMtr). (*L*) 10 Hz thalamocortical stimulation drives a negative fMRI response in iMtr, while 40 Hz stimulation drives a positive fMRI response. (*M*) Peri-event time histograms from a representative unit in iMtr that is inhibited during 10 Hz stimulation ($p=3.4\times10^{-4}$) but excited during 40 Hz stimulation ($p=2.6\times10^{-6}$). (*N*) Quantification of significant changes in firing rate across recorded units in iMtr. (*O*)

Histograms of stimulus-evoked changes in iMtr firing rate ($p=3.9\times10^{-29}$). See also Figure S5.

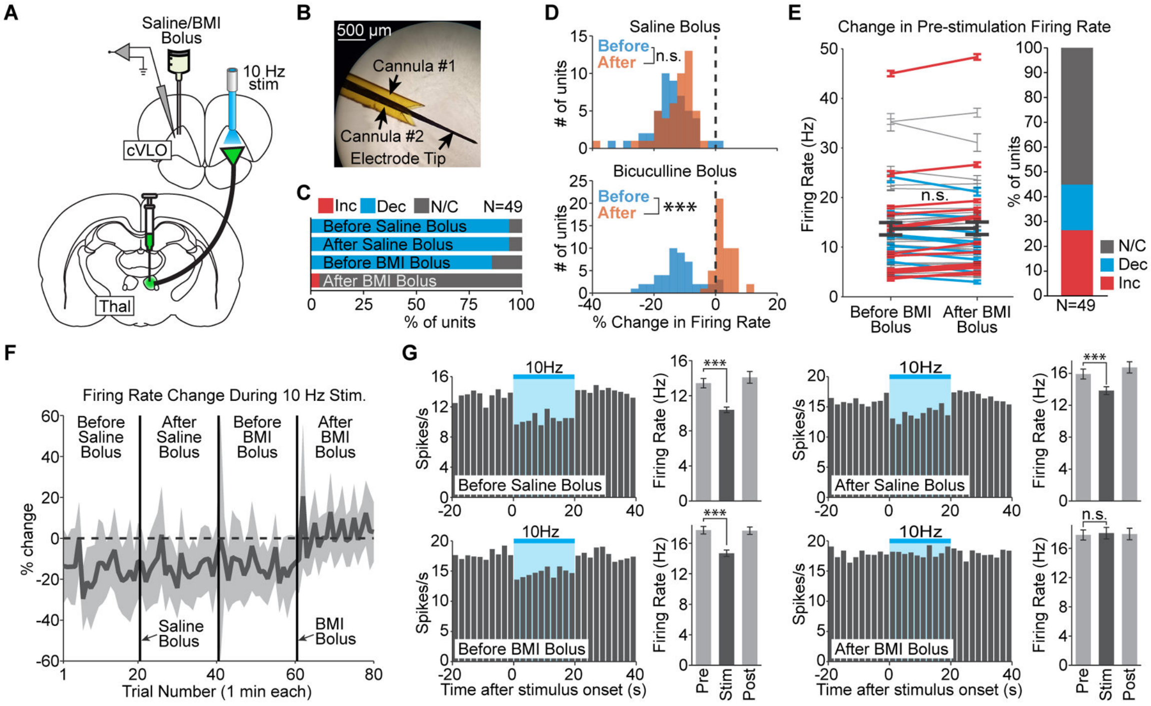

Figure 5. Remote cortical inhibition driven by low-frequency thalamocortical stimulation is mediated by GABA.

(*A*) Schematic of single-unit recording and infusion in cVLO during 10 Hz thalamocortical stimulation. (*B*) Micrograph of the cannula-electrode used to deliver saline and BMI. (*C*) Quantification of significant changes in firing rate during stimulation before and after bolus infusions of saline or BMI. (*D*) Histograms of stimulus-evoked changes in firing rate before and after a single bolus of saline or BMI (p=0.07 and 1.9×10^{-16}, respectively). (*E*) Quantification of baseline firing rate changes after BMI infusion. Error bars represent mean ± s.e.m. over trials for each unit and are color-coded according to whether the unit's baseline firing rate significantly increases or decreases. Thick black line indicates mean ± s.e.m. across units. (*F*) Timeline of stimulus-evoked changes, averaged over all recorded units, during the twenty trials before and after each bolus infusion. Shaded areas represent one standard deviation. Values reflect the percent signal change in firing rate during each trial's 20 s period of stimulation, relative to the preceding 20 s pre-stimulation period. (*G*) Peri-event time histograms from a representative unit in cVLO. The firing rate decreases during 10 Hz stimulation before and after saline infusion (p=2.0×10^{-6} and 1.3×10^{-4}, respectively) and before BMI infusion (p=1.9×10^{-7}). After BMI infusion, 10 Hz stimulation no longer causes a significant change in firing rate (p=0.63). Error bars represent mean ± s.e.m. over trials.

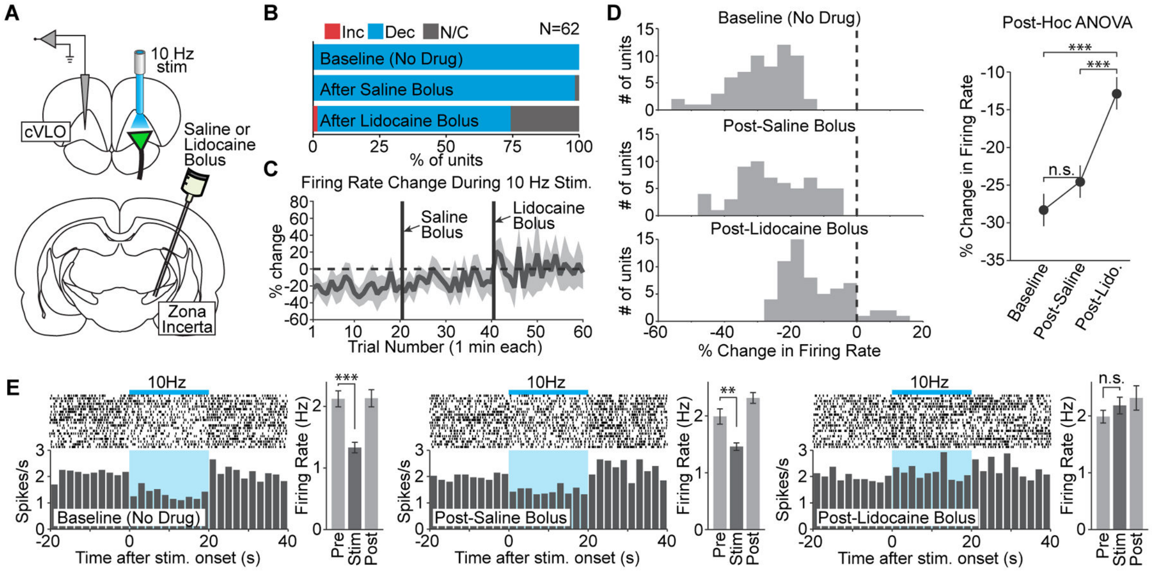

Figure 6. Pharmacological inactivation of zona incerta reduces remote cortical inhibition driven by low-frequency thalamocortical stimulation.

(*A*) Schematic of lidocaine infusion in zona incerta during 10 Hz thalamocortical stimulation and single-unit recordings in cVLO. (*B*) Quantification of significant changes in firing rate evoked by stimulation at baseline and after infusion of saline or lidocaine. (*C*) Timeline of stimulus-evoked changes in firing rate, averaged over units that do not exhibit a significant decrease in firing rate following lidocaine infusion. Shaded areas represent one standard deviation. Values reflect the percent signal change in firing rate during each trial's 20 s period of stimulation, relative to the preceding 20 s pre-stimulation period. (*D*) *Left*, Histograms of stimulus-evoked changes in cVLO firing rate at baseline, post-saline infusion, and post-lidocaine infusion. *Right*, Corresponding group means with 95% confidence intervals and post-hoc ANOVA comparisons (*** $p<0.001$). (*E*) Peri-event time histograms from a representative unit in contralateral VLO. The firing rate decreases during 10 Hz stimulation before and after incertal saline infusion ($p=3.9\times10^{-5}$ and 1.4×10^{-3}, respectively). After lidocaine infusion, the cell no longer exhibits a significant change in firing rate ($p=0.31$). Error bars represent mean ± s.e.m. over trials. See also Figure S7.

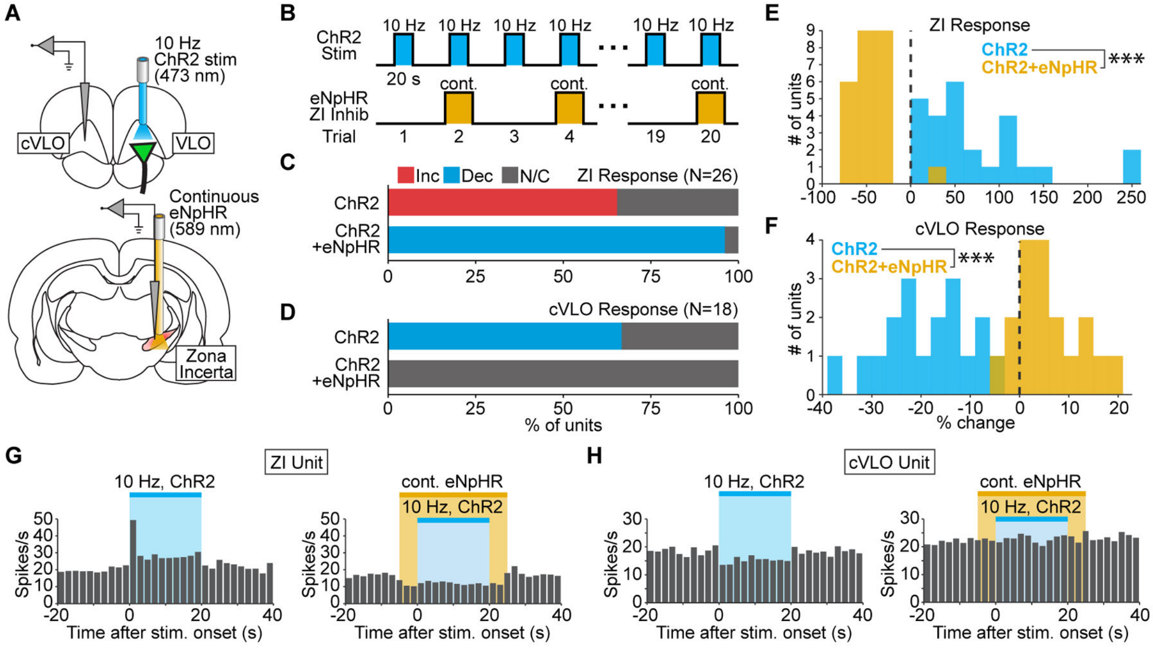

Figure 7. Optical silencing of zona incerta eliminates the remote cortical inhibition driven by low-frequency thalamocortical stimulation.

(*A*) Schematic of single-unit recordings in cVLO and zona incerta (ZI) during 10 Hz thalamocortical stimulation and concurrent silencing of ZI with eNpHR. (*B*) Stimulation paradigm used to assess zona incerta's role in mediating widespread inhibition. (*C*) Quantification of significant changes in ZI firing rate evoked by 10 Hz thalamocortical stimulation with and without eNpHR activation. (*D*) Quantification of significant changes in cVLO firing rate evoked by 10 Hz thalamocortical stimulation with and without incertal silencing. (*E,F*) Histograms of stimulus-evoked changes in ZI (E) and cVLO (F) firing rate ($p=2.2\times10^{-9}$ and 3.8×10^{-7}, respectively). (*G,H*) Peri-event time histograms from representative units in ZI (G) and cVLO (H). The ZI unit's firing rate increases during 10 Hz thalamocortical stimulation ($p=6.1\times10^{-5}$) but decreases when this is paired with eNpHR activation ($p=8.6\times10^{-4}$). The cVLO unit's firing rate decreases during 10 Hz thalamocortical stimulation ($p=0.030$) but does not change when this is paired with eNpHR activation ($p=0.23$). See also Figure S7.

KEY RESOURCES TABLE

REAGENT or RESOURCE	**SOURCE**	**IDENTIFIER**
Antibodies		
Anti-Green Fluorescent Protein	Aves Labs Inc	Part No. GFP-1020; RRID: AB_2307313
Goat anti-Chicken IgY (H+L) Secondary Antibody, Alexa Fluor 568	ThermoFisher Scientific	Part No. A-11041; RRID: AB_2534098
DAPI	ThermoFisher Scientific	Part No. D1306; RRID: AB_2629482
Fluoromount-G	SouthernBiotech	Part No. 0100-01
Bacterial and Virus Strains		
rAAV5-CaMKII-hChR2(H134R)-EYFP	University of North Carolina vector core	Lot AV4316LM
rAAV5-hSyn-eNpHR3.0-mCherry-WPRE	University of North Carolina vector core	Lot AV4834B
Chemicals, Peptides, and Recombinant Proteins		
Bicuculline Methiodide	Sigma-Aldrich	Part No. 14343
Lidocaine Hydrochloride	Fresenius Kabi	Part No. 491507
Feraheme	AMAG Pharmaceuticals	NDC Code 59338-775-01, 59338-775-10
Experimental Models: Organisms/Strains		
Sprague-Dawley	Charles River	Strain Code #001; RRID:RGD_734476
Software and Algorithms		
SPM12	Ashburner et al., 2014	RRID:SCR_007037
NiftyReg	Modat et al., 2010 Modat et al., 2014	RRID:SCR_006593
Matlab	MathWorks	RRID:SCR_001622
OpenEphys Data Collection System	Siegle et al., 2017	http://www.open-ephys.org/gui
OmniPlex Neural Recording Data Acquisition System	Plexon	https://plexon.com/products/omniplex-software/
Wave_Clus	Quiroga et al., 2004	https://github.com/csn-le/wave_clus
Other		
7T Preclinical MRI Scanner	Bruker	BioSpec series; Stanford Center for Innovation in In-Vivo Imaging
Fiber-optic Implant	Duffy et al., 2015 Thorlabs, Inc.	Part No. FT200EMT
Clearfil AP-X Dental Cement	Kuraray Noritake Dental Inc.	Part No. 1721-KA
Electrode Array	NeuroNexus	Part No. 1×16-10mm-100-177
10 uL NanoFil Syringe	World Precision Instruments	Part No. NANOFIL
Infusion cannula	A-M Systems	Part No. 800700
Digital Brain Atlas	Paxinos and Watson, 2006	N/A